Journal of Materials Chemistry B

RSC Publishing

PAPER

View Article Online
View Journal | View Issue



Cite this: J. Mater. Chem. B, 2013, 1, 464

# Phase control of nanostructured iron oxide for application to biosensor†

Rachna Sharma,[ac] Ved Varun Agrawal,*[a] A. K. Srivastava,[a] Govind,[a] Lata Nain,[b] Mohd Imran,[a] Soumya Ranjan Kabi,[b] R. K. Sinha[c] and Bansi D. Malhotra*[d]

We report results of the studies relating to the phase transformation of bare $Fe_3O_4$ nanoparticles (NPs) to $\alpha$-$Fe_2O_3$ NPs obtained during electrophoretic film deposition onto indium-tin oxide coated glass plates. The *in situ* oxidation of NPs during electrophoretic deposition can be circumvented using surface passivation of the $Fe_3O_4$ NPs with an organic shell (carbon) as well as an inorganic shell (silica), while retaining the biocompatibility of the $Fe_3O_4$ NPs. XRD and XPS studies reveal the transformation of $Fe_3O_4$ NPs to $\alpha$-$Fe_2O_3$ NPs upon electrophoretic deposition, and the retention of the phase of the $Fe_3O_4$ NPs upon encapsulation with carbon and silica, respectively. The results of SEM studies indicate decreased agglomeration of the $Fe_3O_4$ NPs upon encapsulation during film deposition. Attempts have been made to compare the characteristics of cholesterol biosensors fabricated using $Fe_3O_4$@C and $\alpha$-$Fe_2O_3$ NPs, respectively. The $Fe_3O_4$@C NPs based cholesterol biosensor shows response time of 60 s, a linearity range of 25–500 mg $dl^{-1}$, a sensitivity of 193 nA $mg^{-1}$ dl $cm^{-2}$ and a Michaelis–Menten constant of 1.44 mg $dl^{-1}$.

Received 1st October 2012
Accepted 9th October 2012

DOI: 10.1039/c2tb00192f

www.rsc.org/MaterialsB

## Introduction

Nanostructured iron oxides ($Fe_3O_4$, $\gamma$-$Fe_2O_3$ and $\alpha$-$Fe_2O_3$) owing to their multifunctional properties, such as small size, superparamagnetism, low toxicity *etc.*, are being widely investigated for applications in high-density information storage,[1] electronic devices,[2] ferrofluid technology,[3] catalysis,[4] pharmaceuticals[5] and biotechnology.[6] Among these, the application of nanostructured iron oxides in clinical diagnostics and biomedicine have aroused much interest because of their biocompatibility and stability under physiological conditions.[7,8] They can also be used as contrast agents in magnetic resonance imaging,[9,10] as mediators in hyperthermia,[11] as carriers for guided drug delivery[12–14] and as immobilization supports for desired biomolecules for the diagnosis of various pathogens and diseases, and estimation of various biochemical analytes such as glucose, urea *etc.*[15–17] Besides this, the particle size of the nanostructured iron oxide can be controlled to a similar size as that of a biomolecule (protein 5–50 nm; virus 20–450 nm; cell 10–100 μm).[18]

Despite several advantages, the susceptibility of $Fe_3O_4$ NPs towards oxidation and their tendency to agglomerate due to strong dipole–dipole attractions between particles, have limited their applications to date.[19] It is anticipated that encasing colloids in a shell of a different material may perhaps protect the core from extraneous chemical and physical changes. Core–shell nanostructures are known to exhibit improved physical and chemical properties over their single-component counterparts, and hence are potentially useful for a range of applications. To improve the stability of the deposited NPs, many molecules, such as carbon and silica, have been considered as interesting encapsulants.[20–22] Compared to polymer and inorganic shells, carbon shells exhibit much higher stability in various chemical and physical environments such as acid or base media, as well as at high temperatures and pressures.[23] Thus, carbon coated $Fe_3O_4$ NPs may perhaps ensure prolonged activity of the biomolecules and enhanced stability of the biosensors.

Among various methods, the formation of nanocrystalline films using electrophoretic deposition has recently gained much interest since it is cost effective[24] and can be used to obtain uniform thin films by optimizing parameters such as solution concentration, applied potential, pH of the solution *etc.*[24,25] The fabrication of nanostructured iron oxide films using electrophoretic deposition and its characterization may perhaps yield important information relating to the phase change of nanostructured iron oxide. Also, the utilization of

[a]National Physical Laboratory, New Delhi-110012, India. E-mail: agrawalvv@nplindia.org; Tel: +91-11-45609489

[b]Division of Microbiology, Indian Agricultural Research Institute, New Delhi-110012, India

[c]Department of Applied Physics, Delhi Technological University, New Delhi-110042, India

[d]Department of Biotechnology, Delhi Technological University, New Delhi-110042, India. E-mail: bansi.malhotra@gmail.com

† Electronic supplementary information (ESI) available: SEM studies showing the immobilization of cholesterol oxidase onto nanostructured iron oxide films, shelf life, reproducibility and response time studies of the fabricated cholesterol biosensors. See DOI: 10.1039/c2tb00192f

nanostructured iron oxide films for the fabrication of biosensors may perhaps result in enhanced electrocatalytic activity of the given biomolecule and improved sensitivity for detection of the desired analyte.

We report a novel method of controlling the phase of iron oxide NPs obtained during electrophoretic deposition. It is shown that the phase of the nanostructured iron oxide during electrophoretic deposition can be tuned to the desired requirements by using bare $Fe_3O_4$ NPs or capped $Fe_3O_4$ NPs as the starting material. The nanocrystalline films of $Fe_3O_4$@C and $\alpha$-$Fe_2O_3$ NPs have been employed for the fabrication of a biosensor using cholesterol oxidase as a model enzyme and the biosensing characteristics have been investigated using electrochemical techniques such as cyclic voltammetry and electrochemical impedance spectroscopy. To the best of our knowledge, there is as yet no report on the phase transformation of $Fe_3O_4$ NPs during electrophoretic deposition, its prevention and further application in biosensing.

## Experimental methods

### Materials and methods

Ferrous sulphate heptahydrate ($FeSO_4 \cdot 7H_2O$), ferric chloride ($FeCl_3$), sodium hydroxide (NaOH), fructose ($C_6H_{12}OH$) powder and tetraethyl orthosilicate ($Si(OC_2H_5)_4$) have been purchased from Sigma-Aldrich. All reagents are of analytical grade and have been used without further purification. De-ionized water (Milli-Q 10 TS) with resistivity >18.2 MΩ cm has been used for preparing all aqueous solutions. Indium-tin-oxide (ITO) coated glass plates have been obtained from Balzers, UK, (Baltracom 247 ITO, 1.1 mm thick) with a sheet resistance and transmittance of 25 Ω $sq^{-1}$ and 90%, respectively. Cholesterol powder and cholesterol oxidase (EC 1.1.36 from *Pseudomonas fluorescens*) with a specific activity of 26 U $mg^{-1}$ have been purchased from Sigma-Aldrich (USA). The stock solution of cholesterol has been prepared in 10% triton X-100 and stored at 4 °C.

### (a) Preparation of $Fe_3O_4$, $Fe_3O_4$@C and $Fe_3O_4$@$SiO_2$ NPs

(i) $Fe_3O_4$ NPs. The $Fe_3O_4$ NPs have been prepared *via* hydrolytic reaction based on chemical co-precipitation of metal salts with an alkali, as reported earlier.[26] Briefly, 0.32 M $FeSO_4 \cdot 7H_2O$ and 0.64 M $FeCl_3$ are added to 10 mL of deoxygenated water (containing 12.1 N HCl) with continuous stirring at 30 °C. The solution containing iron salts is dropwise added to 100 mL of NaOH solution (1.5 M) with vigorous stirring at 30 °C. The mixture is then stirred for an additional 30 min, resulting in the appearance of a black precipitate. The particles are washed by centrifugation at 3500 rpm for 30 min and the supernatant is removed by decantation. The particles are then redispersed in 200 mL of deoxygenated water and are stabilized by making the pH of the sol 3.5 using HCl.

Furthermore, the $Fe_3O_4$ NPs are subjected to high temperature and pressure using autoclaves. 30 mL of the above synthesized NPs are autoclaved at 180 °C for 4 h.[27]

(ii) $Fe_3O_4$@C NPs. Carbon capped $Fe_3O_4$ NPs have been prepared *via* hydrothermal carbonization reaction. For this purpose, 10 mmol of fructose powder is added to 30 mL of $Fe_3O_4$ NPs sol[23,28,29] and the mixture is autoclaved at 180 °C for 4 h. At this temperature, fructose melts and carbonization of fructose occurs, resulting in a carbon shell over the $Fe_3O_4$ NPs.[30] The reaction mixture is cooled under ambient conditions. The synthesized product is washed by centrifugation at 3500 $min^{-1}$ and the supernatant is removed by decantation. No change in color of the sol is observed and the pH of the NPs redispersed in water is recorded as 8.0.

(iii) $Fe_3O_4$@$SiO_2$ NPs. To 10 mL of $Fe_3O_4$ NPs sol (diluted with 40 mL of iso-propanol) are added 1 mL of ammonia and 1 mL of tetraethyl orthosilicate (TEOS).[31] The mixture is stirred at 30 °C for 4 h and a change in colour from dark brown to light brown is observed upon completion of the reaction. The synthesized NPs are collected by centrifugation at 3500 $min^{-1}$ and the pH of the NPs redispersed in water is recorded as 9.6.

### (b) Preparation of nanostructured iron oxide films

The nanocrystalline films of iron oxide are deposited onto ITO coated glass plates using a two-electrode system with platinum as the auxiliary electrode and an ITO-coated glass plate as the deposition electrode. The electrophoretic deposition involves charged particles in a suspension being deposited onto an electrode under the influence of an applied electric field. Thus, the use of surfactant is avoided and the charge on the surface of the NPs is introduced by adjusting the pH of the suspension to obtain a stable sol. The $Fe_3O_4$ NPs carry a positive charge at pH 3.5 since the isoelectric point of $Fe_3O_4$ is 6–7.[32–34] Cationic NPs are deposited onto the ITO-coated glass plate at the cathode terminal. Application of even a small voltage leads to electrolysis of water, producing hydrogen and oxygen gas, which hinder continuous flow of the NPs and affect the film uniformity.[25] Thus, a mixture of methanol–water (2 : 1) is utilized for deposition of the desired nanocrystalline film. The conditions for obtaining uniform films have been optimized for various parameters such as applied potential, concentration, deposition time, *etc.*, and uniform films of $Fe_3O_4$ NPs and $Fe_3O_4$ NPs (autoclaved) are obtained upon application of a 5 V potential for 30 s (Scheme 1).

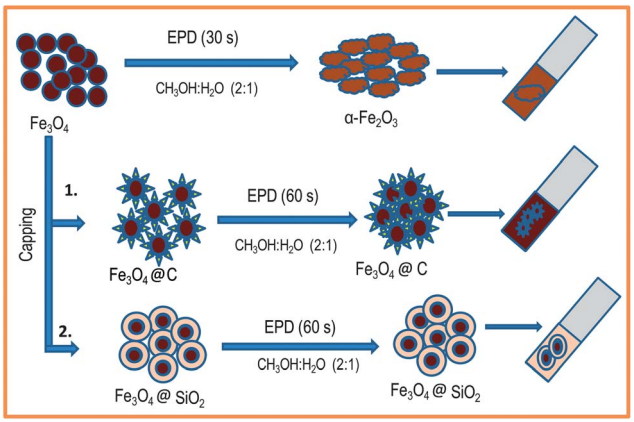


Scheme 1

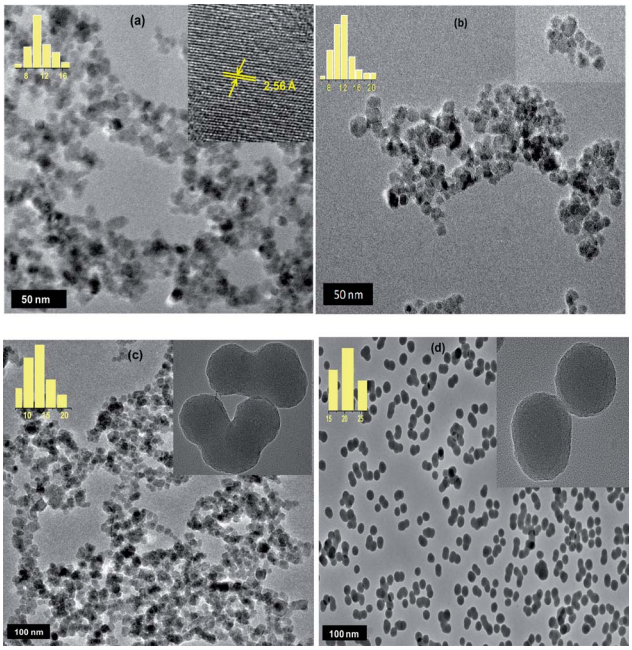


**Fig. 1** TEM micrographs of: (a) $Fe_3O_4$ NPs (inset: high-resolution image of a single particle); (b) $Fe_3O_4$ NPs (autoclaved); (c) $Fe_3O_4$@C NPs; (d) $Fe_3O_4$@$SiO_2$ NPs.

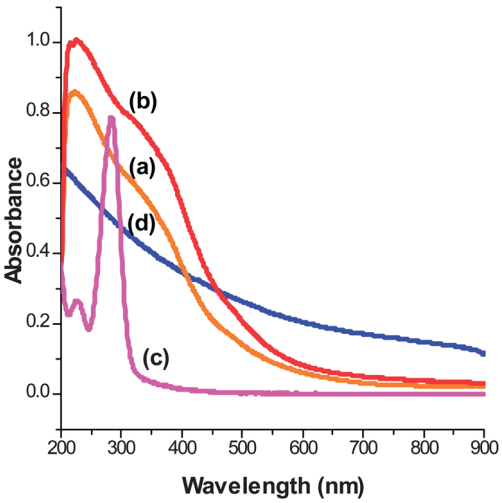


**Fig. 2** UV-vis absorption spectra of: (a) $Fe_3O_4$ NPs; (b) $Fe_3O_4$ NPs (autoclaved); (c) $Fe_3O_4$@C NPs; (d) $Fe_3O_4$@$SiO_2$ NPs.

The $Fe_3O_4$@C and $Fe_3O_4$@$SiO_2$ NPs have been deposited in a methanol–water (2 : 1) mixture. Although the $Fe_3O_4$@C NPs are stable at 8.0 pH, no deposition occurs, indicating that the NPs carry negligible charge. A positive charge on the NPs is then introduced by adjusting the pH to 3.5 and a nanocrystalline film is deposited onto the ITO-coated glass plate at the cathode terminal by applying an optimized potential of 10 V for 60 s. Interestingly, the $Fe_3O_4$@$SiO_2$ NPs carry negative charge at pH 9.6 (as the iso-electric point of $SiO_2$ NPs is ~2),[35] thus a nanocrystalline film is deposited onto the ITO-coated glass plates at the anode terminal upon application of a 10 V potential for 60 s.

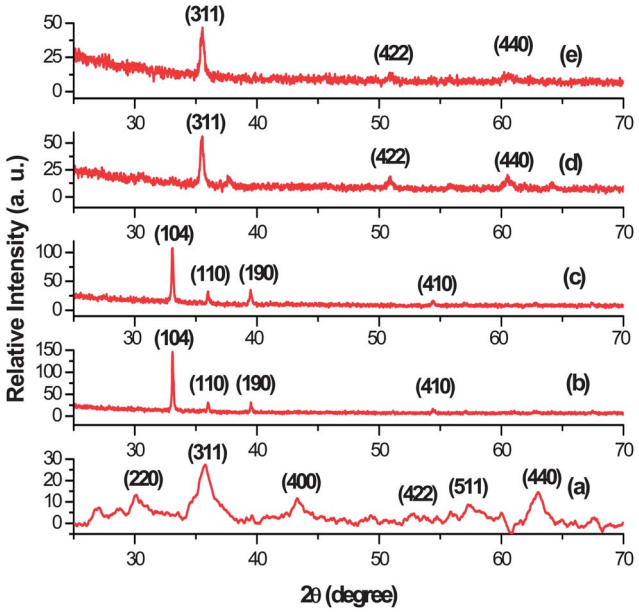


**Fig. 3** XRD spectra of: (a) $Fe_3O_4$ NPs; (b) film obtained from $Fe_3O_4$ NPs; (c) film obtained from $Fe_3O_4$ NPs (autoclaved); (d) film obtained from $Fe_3O_4$@C NPs; (e) film obtained from $Fe_3O_4$@$SiO_2$ NPs.

### (c) Fabrication of nanostructured iron oxide film based bioelectrodes

ChOx is physisorbed onto the nanostructured iron oxide films. For this purpose, 20 μL of freshly prepared ChOx solution (1 mg $mL^{-1}$) is spread onto the α-$Fe_2O_3$ and $Fe_3O_4$@C nanocrystalline films. ChOx immobilized iron oxide films are incubated at 27 °C for 2 h and at 4 °C for 12 h.[36] Later, weakly bound ChOx are removed by washing these films with 100 mM PBS buffer containing 0.05% Tween-20.[37] These films are stored at 4 °C when not in use. The fabricated ChOx/$Fe_3O_4$@C film/ITO and ChOx/α-$Fe_2O_3$ film/ITO bioelectrodes have been characterized *via* SEM, CV and EIS studies and the enzyme activity measurements for the fabricated bioelectrodes have been carried out using CV and EIS techniques.

### (d) Characterization

TEM micrographs have been recorded using a high-resolution transmission electron microscope (HR-TEM, Tecnaii-G2F30 STWIN). Samples for TEM are prepared on 200 mesh carbon coated copper grids. A drop of iron oxide NPs sol is carefully placed on the copper grid surface and is then dried under ambient conditions. The structure of the powder samples and nanostructured iron oxide films have been analyzed using X-ray powder diffraction (XRD, Cu-Kα radiation, Rigaku) over the 2$\theta$ range from 25–70° using a monochromatized X-ray beam with Cu-Kα radiation ($\lambda$ = 1.54 Å). XPS measurements have been carried out in a Perkin Elmer XPS chamber (PHI 1257) with a base pressure of $5 \times 10^{-9}$ torr. The chamber is equipped with a dual anode Mg-$K_\alpha$ (energy 1253.6 eV) and Al-$K_\alpha$ (energy 1486.6 eV) X-ray source and a high-resolution hemispherical energy analyzer for energy resolved electron detection. An Mg-$K_\alpha$ X-ray source has been used for this study. The samples are

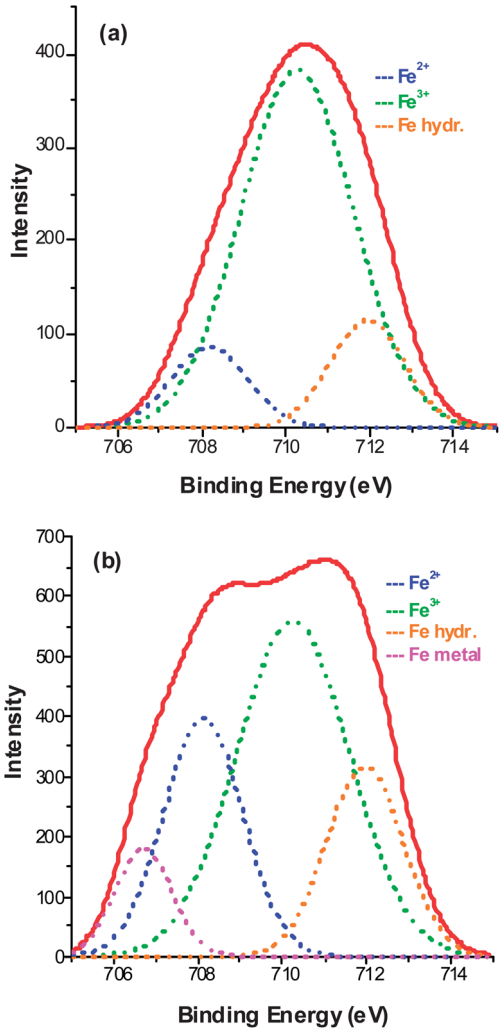


**Fig. 4** Deconvoluted XPS spectra of Fe $2p_{3/2}$ acquired for: (a) $\alpha$-$Fe_2O_3$ film, and (b) $Fe_3O_4$@C film.

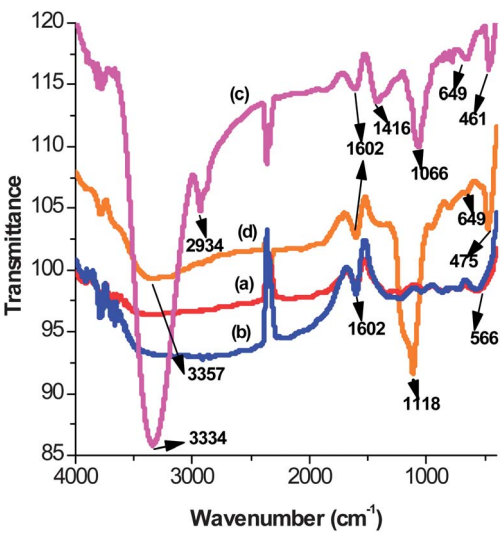


**Fig. 5** FTIR spectra of: (a) $\alpha$-$Fe_2O_3$ NPs film obtained from $Fe_3O_4$ NPs; (b) $\alpha$-$Fe_2O_3$ NPs film obtained from $Fe_3O_4$ NPs (autoclaved); (c) film of $Fe_3O_4$@C NPs; (d) film of $Fe_3O_4$@$SiO_2$ NPs.

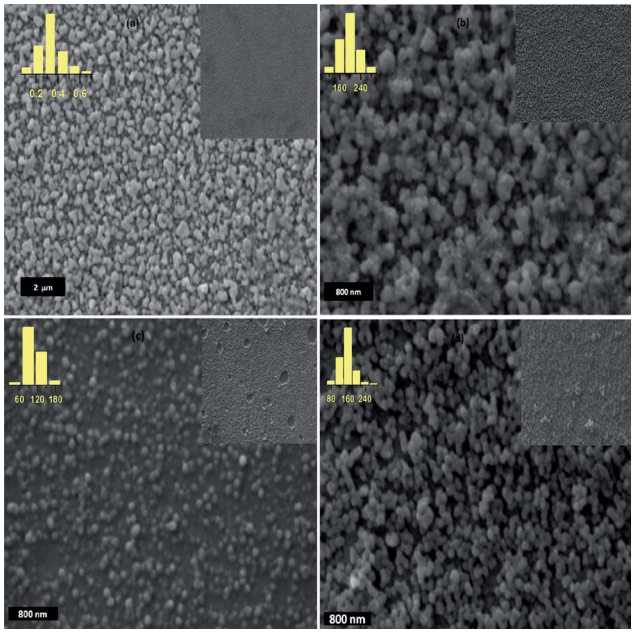

**Fig. 6** SEM micrograph of: (a) $\alpha$-$Fe_2O_3$ NPs film obtained from $Fe_3O_4$ NPs; (b) $\alpha$-$Fe_2O_3$ NPs film obtained from $Fe_3O_4$ NPs (autoclaved); (c) film of $Fe_3O_4$@C NPs; (d) film of $Fe_3O_4$@$SiO_2$ NPs.

sputtered with 4 keV argon ions to remove surface contamination prior to XPS studies. The absorption studies of the bare and encapsulated NPs have been conducted on a Phoenix–2200 DPCV UV-Vis spectrophotometer in the wavelength range 200–900 nm. The transmission studies of the nanostructured iron oxide films in the infrared region have been carried out on a Perkin Elmer, Spectrum BX II spectrophotometer in the wavenumber range of 400–4000 $cm^{-1}$. The morphological changes of the nanocrystalline films upon enzyme immobilization have been studied using SEM (LEO 440 scanning electron microscope).

The electrochemical experiments have been conducted on an Autolab PGSTAT 302N System (Ecochemie, The Netherlands) in a three electrode system. All electrochemical experiments have been carried out in a cell containing 15 mL of 100 mM phosphate buffer solution (PBS) containing 0.9% NaCl and 5 mM $K_3/K_4[Fe(CN)_6]$ as a redox probe and using a platinum wire as auxiliary, a Ag/AgCl wire as reference, and the nanostructured iron oxide films on ITO as the working electrode.

## Results and discussion

### (a) TEM studies of iron oxide NPs

Fig. 1(a) shows a TEM micrograph of the $Fe_3O_4$ NPs, indicating formation of nearly monodispersed nanocrystals with an average diameter of 10 nm. The lattice spacing of ~2.56 Å obtained from the fringe pattern (Inset Fig. 1(a)), matches with the *d*-value (2.56 Å), corresponding to the (311) *hkl* plane of the $Fe_3O_4$ nanocrystals (JCPDS file: 890951). However, after hydrothermal treatment, the average size of the NPs increases by about two nm (Fig. 1(b)). The increase in the average particle size of autoclaved NPs and the decrease in the number of

**Table 1** Optical density of Gram positive (*Providencia* sp.) and Gram negative (*Bacillus* sp.) bacteria as a function of time in the presence of $Fe_3O_4$@C and $\alpha$-$Fe_2O_3$ films

| | | Optical density | | | | | | |
|---|---|---|---|---|---|---|---|---|
| Nanostructured film | Bacteria | 0 h | 2 h | 4 h | 6 h | 8 h | 10 h | 12 h |
| $Fe_3O_4$@C film | *Providencia* sp. | 0.01 | 0.03 | 0.07 | 0.15 | 0.28 | 0.43 | 0.56 |
| $Fe_3O_4$@C film | *Bacillus* sp. | 0.02 | 0.09 | 0.24 | 0.57 | 0.68 | 0.73 | 0.89 |
| $\alpha$-$Fe_2O_3$ film | *Providencia* sp. | 0.03 | 0.06 | 0.09 | 0.14 | 0.19 | 0.54 | 0.63 |
| $\alpha$-$Fe_2O_3$ film | *Bacillus* sp. | 0.02 | 0.08 | 0.26 | 0.58 | 0.65 | 0.82 | 0.85 |

smaller NPs indicates the growth of NPs at the expense of smaller NPs, suggesting Ostwald ripening[38] of NPs. Also, the edges and roughness observed on the NPs' surfaces are reduced upon hydrothermal treatment, and the NPs assume a spherical shape. Thus, the size and smoothness of the NPs can be tailored using hydrothermal treatment.

Upon capping the $Fe_3O_4$ NPs with carbon and silica, the average particle size of the $Fe_3O_4$ NPs increased to 14 nm and 20 nm (Fig. 1(c) and (d)) suggesting the formation of a carbon and silica shell, respectively, over the $Fe_3O_4$ NPs. Due to the formation of the thick shell of silica, the $Fe_3O_4$ NPs are well separated and uniform (inset Fig. 1(d)) while some agglomeration has been observed in the case of the $Fe_3O_4$@C NPs (inset Fig. 1(c)).

### (b) UV-visible studies of $Fe_3O_4$, $Fe_3O_4$ (autoclaved), $Fe_3O_4$@C and $Fe_3O_4$@$SiO_2$ NPs

Fig. 2 shows absorption spectra of the $Fe_3O_4$ NPs, $Fe_3O_4$ NPs (autoclaved), $Fe_3O_4$ NPs capped with carbon and $Fe_3O_4$ NPs capped with silica in the UV-Vis wavelength range. The absorption onset of the $Fe_3O_4$ NPs is at ~600 nm (Fig. 2(a)). Because of the quantum size effect, this onset value is blue-shifted by 100 nm as compared to that of the bulk $Fe_3O_4$.[39] The band near 300 nm corresponds to ligand field transitions of $Fe^{3+}$ and the shoulder peak around 480 nm corresponds to excitation of the Fe–Fe pair.[40] A similar spectrum is observed for the autoclaved $Fe_3O_4$ NPs (Fig. 2(b)). The higher absorption for the autoclaved NPs for the same concentration may be due to an increase in particle size of the NPs upon hydrothermal treatment.

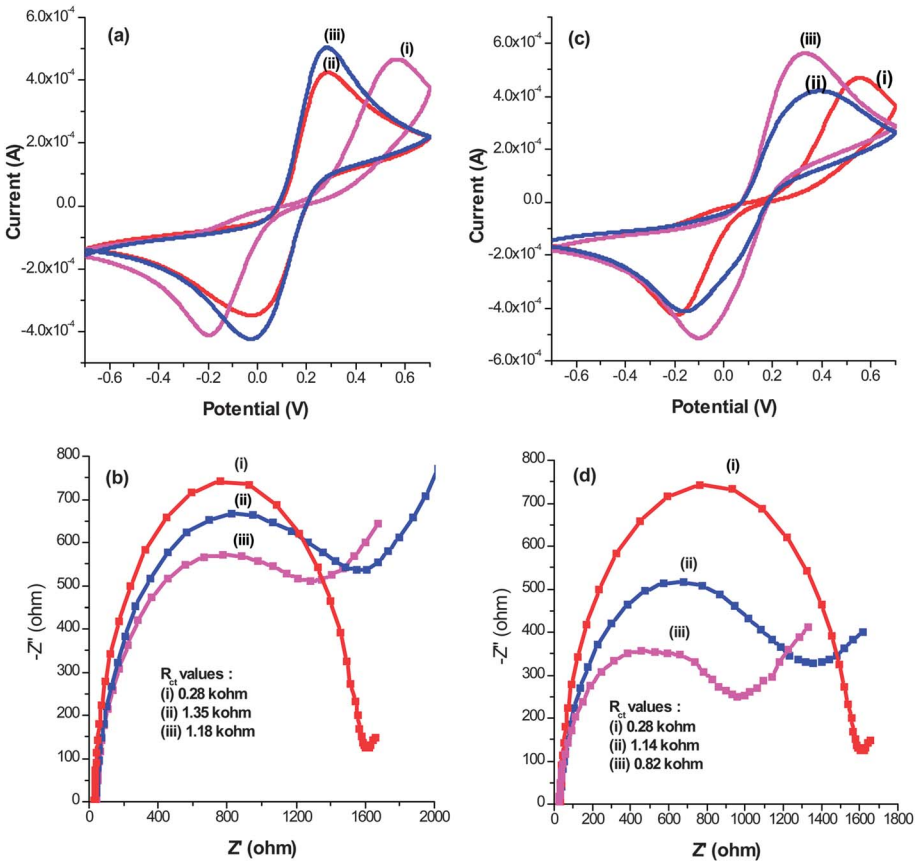


**Fig. 7** (a) CV curves for the ITO electrode (i), $Fe_3O_4$@C film/ITO electrode (ii), and ChOx/$Fe_3O_4$@C film/ITO bioelectrode (iii); (b) Nyquist plots for the ITO electrode (i), $Fe_3O_4$@C film/ITO electrode (ii), and ChOx/$Fe_3O_4$@C film/ITO bioelectrode (iii); (c) CV curves for the ITO electrode (i), $\alpha$-$Fe_2O_3$ film/ITO electrode (ii), and ChOx/$\alpha$-$Fe_2O_3$ film/ITO bioelectrode (iii); (d) Nyquist plots for the ITO electrode (i), $\alpha$-$Fe_2O_3$ film/ITO electrode (ii), and ChOx/$\alpha$-$Fe_2O_3$ film/ITO bioelectrode (iii).

 

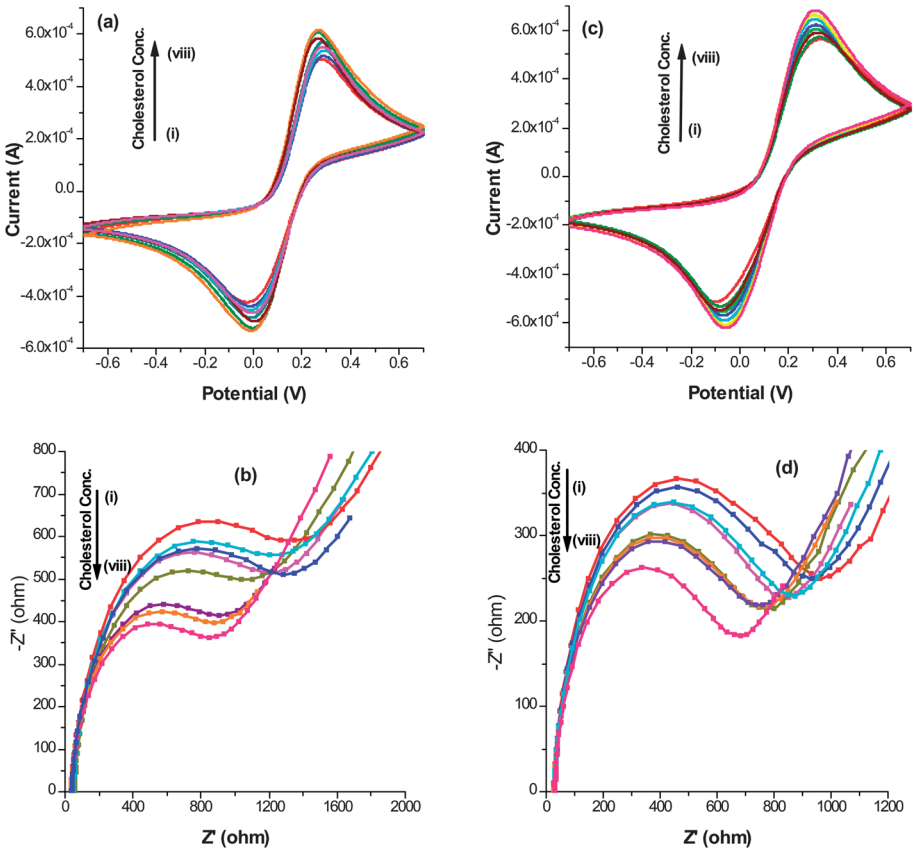


**Fig. 8** (a) CV response studies of ChOx/$Fe_3O_4$@C film/ITO bioelectrode; (b) EIS response studies of ChOx/$Fe_3O_4$@C film/ITO bioelectrode; (c) CV response studies of ChOx/$\alpha$-$Fe_2O_3$ film/ITO bioelectrode and (d) EIS response studies of ChOx/$\alpha$-$Fe_2O_3$ film/ITO bioelectrode with different cholesterol concentrations (mg $dl^{-1}$): (i) 10; (ii) 25; (iii) 50; (iv) 100; (v) 200; (vi) 300; (vii) 400 and (viii) 500.

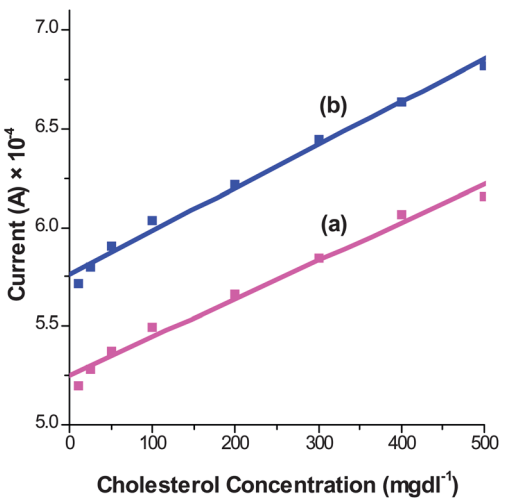


**Fig. 9** Linear calibration plots obtained using CV data for: (a) ChOx/$Fe_3O_4$@C film/ITO bioelectrode and (b) ChOx/$\alpha$-$Fe_2O_3$ film/ITO bioelectrode.

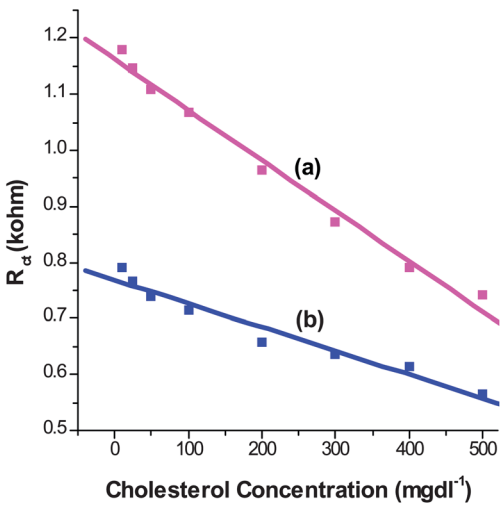


**Fig. 10** Linear calibration plots obtained using EIS data for: (a) ChOx/$Fe_3O_4$@C film/ITO bioelectrode and (b) ChOx/$\alpha$-$Fe_2O_3$ film/ITO bioelectrode.

Upon encapsulation of the $Fe_3O_4$ NPs with carbon and silica shells, the scattering from the NPs increases due to an increase in particle size.[41] Importantly, this increase in scattering is specific to the wavelength range of 500–900 nm. On the contrary, the absorption at lower wavelengths is suppressed due to capping of the $Fe_3O_4$ NPs. Such crossover in absorption spectra for the same concentration suggests surface modification of the $Fe_3O_4$ NPs. For the carbon capped $Fe_3O_4$ NPs, the characteristic spectrum from the $Fe_3O_4$ NPs is retained (Fig. 2(c)), but the partial suppression of the absorption

**Table 2** Comparison table summarizing the characteristics of cholesterol biosensors based on nanostructured metal oxide films

| Electrode | Transducer | Linear range (mg $dL^{-1}$) | Sensitivity | $K_m$ value | Response time (s) | Reproducibility | Shelf life (days) | Ref. |
|---|---|---|---|---|---|---|---|---|
| $CeO_2$/ITO | Cyclic voltammetry | 10–400 | — | 2.08 mM | 15 | — | — | 62 |
| Chitosan–$SnO_2$/ITO | Cyclic voltammetry | 5–400 | 34.7 μA $mg^{-1}$ dl $cm^{-2}$ | 3.8 mM | 5 | — | 80 | 63 |
| ZnO/Au | Cyclic voltammetry | 25–400 | 45.7 nA $mg^{-1}$ dl $cm^{-2}$ | 2.1 mM | 15 | — | 70 | 64 |
| ZnO/ITO | Cyclic voltammetry | 5–400 | 59.0 nA $mg^{-1}$ dl $cm^{-2}$ | 0.03 mM | 10 | 20 | 85 | 65 |
| $Fe_3O_4$ NPs | Spectroscopy | 50–200 | — | 0.45 mM | — | — | 10 | 66 |
| $Fe_3O_4$@C/ITO | Cyclic voltammetry<br>Impedance spectroscopy | 25–400 | 193 nA $mg^{-1}$ dL $cm^{-2}$<br>0.90 Ω $mg^{-1}$ dL $cm^{-2}$ | 0.03 mM | 60 | 25 | 70 | Present work |
| α-$Fe_2O_3$/ITO | Cyclic voltammetry<br>Impedance spectroscopy | 50–400 | 218 nA $mg^{-1}$ dL $cm^{-2}$<br>0.42 Ω $mg^{-1}$ dL $cm^{-2}$ | 0.04 mM | 60 | 20 | 56 | |

intensity suggests the capping of the $Fe_3O_4$ NPs with a thin layer of carbon. Upon capping the $Fe_3O_4$ NPs with silica, an absence of the characteristic absorption from $Fe_3O_4$ NPs (200–450 nm) can be seen[42,43] (Fig. 2(d)). This suggests complete coverage of the $Fe_3O_4$ NPs with a thick shell of silica, which increases the overall scattering from the NPs, while on the contrary, it completely suppresses the absorption from the $Fe_3O_4$ NPs.

### (c) X-Ray diffraction studies of $Fe_3O_4$ NPs and nanostructured iron oxide films

Fig. 3(a) shows an XRD pattern of the bare $Fe_3O_4$ NPs. The diffraction peaks obtained correspond to the cubic spinel structure of $Fe_3O_4$.[44,45] The average particle diameter of 10.6 nm calculated using the Debye–Scherrer formula (from the most intense peak at $2\theta = 35.57^\circ$) is in agreement with the particle size determined by statistical analysis of the TEM images, indicating that each individual particle is a single crystal.[46]

Fig. 3(b) and (c) show XRD spectra of the iron oxide films prepared from the $Fe_3O_4$ NPs and $Fe_3O_4$ NPs (autoclaved), respectively. The diffraction peaks of the films match α-$Fe_2O_3$ (JCPDS file: 890599-96). In spite of the $Fe_3O_4$ NPs being the starting material for the film deposition, the XRD spectra obtained from the deposited film corresponds to that of α-$Fe_2O_3$. This change of phase can be ascribed to the oxidation of NPs during electrophoretic deposition in the water–methanol mixture. The hydroxyl (OH) groups resulting from the dissociation of water and methanol molecules get adsorbed on the surface of magnetite NPs and catalyze their oxidation process.[47] In addition, the application of a potential above the oxidation potential of $Fe^{2+}$ (*i.e.* 0.77 V) results in the modified nucleation rate (kinetics), enhanced diffusion of species and gradient of the lattice constant, which drives the nucleation of α-$Fe_2O_3$ NPs.[47,48] Also, uncapped $Fe_3O_4$ NPs undergo rapid agglomeration during deposition, their large size favors the oxidation to hematite over magnetite.[49] To the best of our knowledge, a change in phase of $Fe_3O_4$ NPs obtained during electrophoretic deposition occurring in such a short span of time (30 s) has not been reported in the literature.

To control this oxidation step, the $Fe_3O_4$ NPs have been encapsulated with an organic carbon shell and an inorganic silica shell, as mentioned in the preceding section. Fig. 3(d) and (e) show XRD spectra of the films obtained from the $Fe_3O_4$@C NPs and $Fe_3O_4$@$SiO_2$ NPs, respectively. The diffraction peaks obtained from the films of the encapsulated NPs match those of $Fe_3O_4$ (with a slight shift), indicating that no oxidation occurs during the deposition of films upon capping the $Fe_3O_4$ NPs with organic and inorganic shells. After capping, the surface of the $Fe_3O_4$ NPs has been passivated, which circumvents the adsorption of hydroxyl groups onto their surface and thus prevents their phase change. Thus, an additional oxidation step during electrophoretic deposition of $Fe_3O_4$ NPs can be circumvented using surface passivation.

### (d) X-Ray photoelectron studies of α-$Fe_2O_3$ and $Fe_3O_4$@C films

To further confirm the phase of the NPs before and after electrophoretic deposition, XPS core level spectra of α-$Fe_2O_3$ and $Fe_3O_4$@C films have been acquired for Fe 2p and the deconvoluted Fe $2p_{3/2}$ spectra are shown in Fig. 4. Background subtraction and peak fitting of the spectra have been done using the Shirley function and Gaussian function, respectively, and the spectra have been referenced to the C 1s main peak at 284.6 eV. A considerable difference can be seen in the two spectra for the α-$Fe_2O_3$ and $Fe_3O_4$@C films.

Fig. 4(a) shows the deconvoluted XPS Fe $2p_{3/2}$ spectra of the α-$Fe_2O_3$ film. The peak fitting of the spectra reveals that $Fe^{2+}$ and $Fe^{3+}$ ions are present in the ratio of 1 : 6.7. This shows that the film mostly contains $Fe_2O_3$ with traces of $Fe_3O_4$, which suggests the *in situ* oxidation of uncapped $Fe_3O_4$ NPs during electrophoretic deposition. However, the deconvolution and peak fitting of the Fe $2p_{3/2}$ spectra obtained for the $Fe_3O_4$@C film reveals that the ratio of $Fe^{2+}$ and $Fe^{3+}$ ions is 1 : 2 (Fig. 4(b)). This shows that the $Fe_3O_4$ NPs retain their phase upon encapsulation with carbon and the film consists of $Fe_3O_4$ NPs. Thus, surface passivation restricts the *in situ* oxidation of $Fe_3O_4$ NPs during electrophoretic deposition. The presence of metal Fe has also been noticed in $Fe_3O_4$@C film, while hydrated Fe is present in both the films, as expected.[50,51]

### (e) FTIR studies of nanostructured iron oxide films

Fig. 5 shows the transmittance spectra of the nanostructured iron oxide films. In the case of the α-$Fe_2O_3$ NPs film (Fig. 5(a) and (b)) (obtained from $Fe_3O_4$ NPs and $Fe_3O_4$ NPs (autoclaved),

 

respectively), the peak seen at 566 $cm^{-1}$ corresponds to the vibrations of Fe–O.[19] However, upon capping of the $Fe_3O_4$ NPs with carbon and silica, the Fe–O vibration peak at 566 $cm^{-1}$ disappears and two additional peaks at 649 $cm^{-1}$ and 465 $cm^{-1}$ (Fig. 5(c) and (d)) have been obtained.

In the case of the carbon capped $Fe_3O_4$ NPs (Fig. 5(c)), the peak at 2934 $cm^{-1}$ refers to the C–H stretching vibrations, the peak at 1416 $cm^{-1}$ refers to the C–H bending vibrations and the peak at 1066 $cm^{-1}$ refers to the C–O stretching vibrations. All these peaks indicate the presence of aliquots of fructose, since fructose molecules present in the hydrated state are unlikely to decompose completely,[52–54] but as a convention adopted by previous reports, we label these nanoparticles as carbon capped $Fe_3O_4$ NPs.[23,29]

In the case of silica capped $Fe_3O_4$ NPs (Fig. 5(d)), a sharp peak at 1118 $cm^{-1}$ corresponds to characteristic Si–O vibrations, revealing the capping of the $Fe_3O_4$ NPs with silica.[55,56] The broad band found at 3300–3400 $cm^{-1}$ and the peak at 1602 $cm^{-1}$ present in all the films correspond to the O–H stretching mode and the H–O–H bending mode, respectively, indicating the presence of interstitial water molecules in the films.[44]

### (f) Morphological studies of nanostructured iron oxide films and bioelectrodes

Fig. 6 shows the SEM micrographs of the nanostructured iron oxide films. It can be seen that the $\alpha$-$Fe_2O_3$ films obtained from $Fe_3O_4$ NPs and $Fe_3O_4$ NPs (autoclaved) have an average particle size of 300 nm and 200 nm, respectively (Fig. 6(a) and (b)). The observed increase in particle size and deformation in shape indicate agglomeration of the uncapped NPs upon deposition. The agglomeration is more prominent for the as-prepared $Fe_3O_4$ NPs owing to their surface roughness. The electrical double layer gradient is maximum at the edges of the NPs, which results in the electrostatic attraction of the NPs and the growth in their size.[57] However, due to the removal of edges and surface smoothing of the NPs upon hydrothermal treatment, the autoclaved NPs undergo reduced aggregation.

Upon capping of the $Fe_3O_4$ NPs with carbon and silica, the agglomeration has been further restricted. A radical decrease of the average particle size to 100 nm (Fig. 6(c)) and 160 nm (Fig. 6(d)) is observed in the case of the carbon capped NPs and silica capped NPs, respectively. Also, the capped NPs retain their initial spherical shape upon deposition, as compared to the film of uncapped NPs. The reduction in size and retention of spherical shape indicate a considerable decrease in the agglomeration of NPs upon capping. Further, the immobilization of cholesterol oxidase onto the nanostructured iron oxide films has been confirmed using SEM (Fig. S1, ESI†). The change in morphology from a dense uniform distribution of NPs in the nanoscale to the globular structure of ChOx at the micron scale is attributed to the physical adsorption of ChOx molecules onto nanostructured iron oxide films.[58]

### (g) Biocompatibility of $Fe_3O_4$@C and $\alpha$-$Fe_2O_3$ films

The biocompatibility of the $Fe_3O_4$@C and $\alpha$-$Fe_2O_3$ films has been investigated using bacterial systems *i.e.* Gram positive (*Bacillus* sp.) and Gram negative (*Providencia* sp.) bacteria. Two methods have been utilized to examine the biocompatibility of nanostructured iron oxide films. Firstly, cultures of Gram positive and Gram negative bacteria are spread on nutrient agar plates and $Fe_3O_4$@C and $\alpha$-$Fe_2O_3$ films are kept on these plates under optimum growth conditions (28 °C and 150 rpm). No zone of inhibition is observed for the nanostructured iron oxide films. Secondly, side arm flasks are prepared with nutrient broth and both the bacteria are inoculated. Films are kept in the nutrient broth and grown under optimum conditions (28 °C and 150 rpm). Colorimetric readings recorded at intervals of 2 h are summarized in Table 1, which clearly indicates the biocompatibility of the $Fe_3O_4$@C and $\alpha$-$Fe_2O_3$ films as the optical density of Gram positive and Gram negative bacteria increases with time in the presence of nanostructured iron oxide films.

### (h) Electrochemical characterization of ChOx immobilized iron oxide electrodes

(i) ChOx/$Fe_3O_4$@C film/ITO bioelectrode. Fig. 7(a) shows the cyclic voltammograms of the ITO electrode, $Fe_3O_4$@C film/ITO electrode and ChOx/$Fe_3O_4$@C film/ITO bioelectrode in the potential range of −0.7 V to +0.7 V at a scan rate of 30 mV $s^{-1}$. The decrease in anodic peak current obtained for the $Fe_3O_4$@C film/ITO electrode (Fig. 7(a), (ii)) compared to that of the ITO electrode (Fig. 7(a), (i)) reveals the formation of a layer of $Fe_3O_4$@C NPs on the ITO surface. Furthermore, the increase in oxidation current obtained for the ChOx/$Fe_3O_4$@C film/ITO bioelectrode (Fig. 7(a), (iii)) compared to that of the $Fe_3O_4$@C film/ITO electrode (Fig. 7(a), (ii)) is attributed to electron transfer facilitated by redox moieties at the active sites (FAD centres) of the enzyme at the electrode surface.

Fig. 7(b) shows the Nyquist plots obtained for the ITO electrode, $Fe_3O_4$@C film/ITO electrode and ChOx/$Fe_3O_4$@C film/ITO bioelectrode. The increased $R_{ct}$ value of 1.35 kΩ for the $Fe_3O_4$@C film/ITO electrode (Fig. 7(b), (ii)) compared to the $R_{ct}$ value of 0.28 kΩ for the ITO electrode (Fig. 7(b), (i)) indicates formation of a $Fe_3O_4$@C NPs layer on the ITO surface. The presence of the $Fe_3O_4$@C NPs layer impedes the flow of electrons, resulting in an increased value of $R_{ct}$. Furthermore, a decrease in $R_{ct}$ value from 1.35 kΩ for the $Fe_3O_4$@C film/ITO electrode to 1.18 kΩ for the ChOx/$Fe_3O_4$@C film/ITO bioelectrode (Fig. 7(b), (iii)) reveals the ChOx immobilization onto the $Fe_3O_4$@C film/ITO electrode. This decrease in $R_{ct}$ value is ascribed to the facile electron transfer aided by the redox moieties of the enzyme at the electrode surface.

According to Laviron's theory, the slope of the linear curve between the anodic peak potential and the logarithm of scan rate represents $RT/\alpha nF$ ($\alpha$: transfer coefficient). This can be used to calculate the surface concentration of the ionic species of the bioelectrodes using the following equation:

$$i_p = n^2F^2\nu CA(4RT)^{-1} \quad (1)$$

where, $i_p/\nu$ can be calculated from the $i_p$ *vs.* $\nu$ plot[58] ($i_p$: anodic peak current; $\nu$: scan rate).

The slope of the linear plot of anodic peak potential *vs.* logarithm of scan rate for the ChOx/$Fe_3O_4$@C film/ITO

bioelectrode gives $RT/\alpha nF = 0.23$. Using eqn (1), the surface concentration on the ChOx/$Fe_3O_4$@C film/ITO bioelectrode has been found to be $2.52 \times 10^{-11}$ mol $cm^{-2}$.

(ii) ChOx/$\alpha$-$Fe_2O_3$ film/ITO bioelectrode. Fig. 7(c) shows the cyclic voltammograms obtained for the ITO electrode, $\alpha$-$Fe_2O_3$ film/ITO electrode and ChOx/$\alpha$-$Fe_2O_3$ film/ITO bioelectrode in the potential range of $-0.7$ V to +0.7 V at a scan rate of 30 mV $s^{-1}$. The oxidation peak seen at 0.38 V is attributed to the oxidation of the redox couple $K_3/K_4[Fe(CN)_6]$, present in the buffer.[58] The decrease in the oxidation current obtained for the $\alpha$-$Fe_2O_3$ film/ITO electrode (Fig. 7(c), (ii)) compared to that of the ITO electrode (Fig. 7(c), (i)) indicates formation of a layer of $\alpha$-$Fe_2O_3$ NPs on the ITO surface. Furthermore, the increase in oxidation current obtained for the ChOx/$\alpha$-$Fe_2O_3$ film/ITO bioelectrode (Fig. 7(c), (iii)) compared to that of the $\alpha$-$Fe_2O_3$ film/ITO electrode (Fig. 7(c), (ii)) is attributed to the presence of redox moieties at active sites (FAD centres) of the enzyme, leading to fast electron transfer between the enzyme and the electrode surface.[37]

Fig. 7(d) shows the Nyquist plots obtained for the ITO electrode, $\alpha$-$Fe_2O_3$ film/ITO electrode and ChOx/$\alpha$-$Fe_2O_3$ film/ITO bioelectrode. The increased $R_{ct}$ (charge transfer resistance) value of 1.14 kΩ obtained for the $\alpha$-$Fe_2O_3$ film/ITO electrode (Fig. 7(d), (ii)) compared to the $R_{ct}$ value of 0.28 kΩ for the ITO electrode (Fig. 7(d), (i)) is attributed to the formation of a layer of $\alpha$-$Fe_2O_3$ NPs on the ITO surface. Formation of an $\alpha$-$Fe_2O_3$ NPs layer results in decreased interfacial electron transfer, thereby causing an increase in the $R_{ct}$ value. Furthermore, the observed decrease in $R_{ct}$ value from 1.14 kΩ for the $\alpha$-$Fe_2O_3$ film/ITO electrode (Fig. 7(d), (ii)) to 0.82 kΩ for the ChOx/$\alpha$-$Fe_2O_3$ film/ITO bioelectrode (Fig. 7(d), (iii)) is attributed to facile electron transfer mediated by the redox centres of the enzyme.

The surface concentration of ionic species on the ChOx/$\alpha$-$Fe_2O_3$ film/ITO bioelectrode has been found to be $1.81 \times 10^{-11}$ mol $cm^{-2}$ (using $RT/\alpha nF = 0.16$). The higher concentration of ionic species on the ChOx/$Fe_3O_4$@C film/ITO bioelectrode compared to the ChOx/$\alpha$-$Fe_2O_3$ film/ITO bioelectrode is attributed to the larger surface area provided by the $Fe_3O_4$@C nanocrystalline film owing to the smaller particle size of the NPs as compared to the $\alpha$-$Fe_2O_3$ nanocrystalline film for enzyme immobilization.

### (i) Electrochemical response of ChOx immobilized iron oxide electrodes

(i) ChOx/$Fe_3O_4$@C film/ITO bioelectrode. Fig. 8(a) shows the response of the ChOx/$Fe_3O_4$@C film/ITO bioelectrode obtained as a function of cholesterol concentration using cyclic voltammetry. The bioelectrode exhibits a response time of 60 s (Fig. S4(a)†). The anodic peak current of the ChOx/$Fe_3O_4$@C film/ITO bioelectrode plotted as a function of cholesterol concentration (Fig. 9(a)) reveals the linearity range as 25–500 mg $dl^{-1}$ with a standard deviation and correlation coefficient of 4.82 μA and 0.99, respectively. The sensitivity of the ChOx/$Fe_3O_4$@C film/ITO bioelectrode exhibited by the slope of the linear regression curve is 193 nA $mg^{-1}$ dl $cm^{-2}$. The value of the Michaelis–Menten constant of the ChOx immobilized $Fe_3O_4$@C film has been found to be 1.44 mg $dl^{-1}$.

The Nyquist plots for the ChOx/$Fe_3O_4$@C film/ITO bioelectrode as a function of cholesterol concentration have been investigated to obtain the impedimetric response of the biosensor (Fig. 8(b)). The linear calibration curve obtained by plotting the $R_{ct}$ value for the ChOx/$Fe_3O_4$@C film/ITO bioelectrode as a function of cholesterol concentration (Fig. 10(a)) reveals a linearity range of 25–500 mg $dl^{-1}$ with standard deviation and regression coefficient of 0.02 kΩ and 0.99, respectively. The sensitivity of 0.90 Ω $mg^{-1}$ dl $cm^{-2}$ is obtained from the slope of the linear regression curve of the ChOx/$Fe_3O_4$@C film/ITO bioelectrode.

The shelf life and reproducibility of the ChOx/$Fe_3O_4$@C film/ITO bioelectrode have been investigated using cyclic voltammetry. The activity of the bioelectrode is monitored at regular intervals of seven days. The bioelectrode exhibits only 6% reduction in peak current after 10 weeks for 100 mg $dl^{-1}$ cholesterol concentration when stored at 4 °C (Fig. S2(a)†). The reproducibility of the sensing parameters of the bioelectrode has been studied with a cholesterol concentration of 25 mg $dl^{-1}$ and it has been found that the bioelectrode can be used up to 25 times without significant decrease (40 μA) of the response signal (Fig. S3(a)†).

(ii) ChOx/$\alpha$-$Fe_2O_3$ film/ITO bioelectrode. Fig. 8(c) shows the response of the ChOx/$\alpha$-$Fe_2O_3$ film/ITO bioelectrode obtained as a function of cholesterol concentration using the cyclic voltammetric technique. The response time of this electrode is found to be 60 s (Fig. S4(b)†). The magnitude of the amperometric current of the ChOx/$\alpha$-$Fe_2O_3$ film/ITO bioelectrode plotted as a function of cholesterol concentration (Fig. 9(b)) shows linearity in the range 25–500 mg $dl^{-1}$ with standard deviation and correlation coefficient of 4.52 μA and 0.99, respectively. The sensitivity of the ChOx/$\alpha$-$Fe_2O_3$ film/ITO bioelectrode exhibited by the slope of linear calibration curve is found to be 218 nA $mg^{-1}$ dl $cm^{-2}$. The value of the Michaelis–Menten constant of the ChOx immobilized $\alpha$-$Fe_2O_3$ film has been found to be 1.46 mg $dl^{-1}$.

The electrochemical impedimetric response of the ChOx/$\alpha$-$Fe_2O_3$ film/ITO bioelectrode has been investigated as a function of cholesterol concentration using Nyquist plots (Fig. 8(d)). The linear calibration curve obtained by plotting the $R_{ct}$ values for the ChOx/$\alpha$-$Fe_2O_3$ film/ITO bioelectrode as a function of cholesterol concentration (Fig. 10(b)) reveals a linearity range of 50–500 mg $dl^{-1}$ with standard deviation and regression coefficient of 0.02 kΩ and 0.97, respectively. The value of sensitivity exhibited by the slope of the linear regression curve for the ChOx/$\alpha$-$Fe_2O_3$ film/ITO bioelectrode is 0.42 Ω $mg^{-1}$ dl $cm^{-2}$ (Table 2).

The shelf-life of the ChOx/$\alpha$-$Fe_2O_3$ film/ITO bioelectrode has been investigated for a 100 mg $dl^{-1}$ cholesterol concentration using cyclic voltammetry. The bioelectrode exhibits a 6% decrease in the peak current for the first 8 weeks, but a sudden decrease in the signal has been observed afterwards and the current reduced by 11.5% after 10 weeks (Fig. S2(b)†). The ChOx/$\alpha$-$Fe_2O_3$ film/ITO bioelectrode can be used up to 20 times with insignificant loss (66 μA) of the signal (Fig. S3(b)†).

 

## Conclusions

Nanocrystals of $Fe_3O_4$ with an average particle diameter of 10 nm have been synthesized. The electrophoretic deposition of bare $Fe_3O_4$ NPs in a methanol–water mixture results in oxidation and phase transformation of NPs and a film of $\alpha$-$Fe_2O_3$ NPs has been obtained. The phase transformation of the $Fe_3O_4$ NPs can be circumvented using surface passivation of $Fe_3O_4$ NPs with an organic carbon shell and an inorganic silica shell. Encapsulation of the $Fe_3O_4$ NPs restricts agglomeration of NPs during film deposition and retains a high surface to volume ratio for enzyme loading. Due to the non-conducting nature of silica, $Fe_3O_4$@$SiO_2$ NPs show poor electrochemical response. However, these can be utilized for applications in drug delivery,[21] biocatalysis and bioseparation,[20,59] magnetic resonance imaging,[60] determination of metal ion concentration,[61] *etc.* Growth of Gram positive and Gram negative bacteria in contact with the $Fe_3O_4$@C and $\alpha$-$Fe_2O_3$ films reveals the biocompatible nature of the nanostructures, which is suitable for prolonged activity of enzymes and thus, stability of biosensors. The fabricated cholesterol biosensors employing $Fe_3O_4$@C and $\alpha$-$Fe_2O_3$ nanocrystalline films show sensitivities of 193 nA $mg^{-1}$ dl $cm^{-2}$ and 218 nA $mg^{-1}$ dl $cm^{-2}$, respectively, from cyclic voltammetric studies and sensitivities of 0.42 Ω $mg^{-1}$ dl $cm^{-2}$ and 0.90 Ω $mg^{-1}$ dl $cm^{-2}$, respectively, from electrochemical impedance spectroscopic studies. The low values of the Michaelis–Menten constant reveals the enhanced enzymatic activity of ChOx on nanostructured iron oxide films. The comparable sensitivities for biosensors obtained using $Fe_3O_4$@C and $\alpha$-$Fe_2O_3$ NPs suggests that encapsulation of $Fe_3O_4$ NPs with carbon does not significantly affect the electrocatalytic activity of $Fe_3O_4$ NPs, while it adds to the stability of the NPs. However, the encapsulation of $Fe_3O_4$ NPs with conjugated carbon molecules, conducting polymers like polypyrrole, polyaniline, *etc.*, may result in improved sensitivity of the biosensor.

## Acknowledgements

We thank Prof. R. C. Budhani, Director, National Physical Laboratory, New Delhi, India for providing facilities. R. S. is thankful to the UGC-CSIR for the award of a Junior Research Fellowship. The authors thank Dr K. N. Sood, NPL for SEM measurements, Dr S. M. Shivprasad, JNCASR for XPS measurements and Dr Kavita Arora, JNU for TEM studies. Financial support received from the Department of Science and Technology (DST) centre on biomolecular electronics and CSIR Empower projects is sincerely acknowledged. Thanks are due to Dr Pratima Solanki, C. M. Pandey, Manoj Patel and all the members of the Biomedical Instrumentation Section, NPL, for discussions.

## References

1 S. Chou, *J. Appl. Phys.*, 1994, **76**, 6673.
2 D. Schaadt, *J. Vac. Sci. Technol., A*, 2000, **18**, 1834.
3 K. Mosbach and L. Andersson, *Nature*, 1977, **270**, 259–261.
4 D. K. Yi, S. S. Lee and J. Y. Ying, *Chem. Mater.*, 2006, **18**, 2459–2461.
5 C. B. Catherine and S. G. C. Adam, *J. Phys. D: Appl. Phys.*, 2003, **36**, R198.
6 E. Amstad, M. Textor and E. Reimhult, *Nanoscale*, 2011, **3**, 2819–2843.
7 S. Laurent, D. Forge, M. Port, A. Roch, C. Robic, L. Vander Elst and R. N. Muller, *Chem. Rev.*, 2008, **108**, 2064–2110.
8 T. Osaka, T. Matsunaga, T. Nakanishi, A. Arakaki, D. Niwa and H. Iida, *Anal. Bioanal. Chem.*, 2006, **384**, 593–600.
9 R. Weissleder, H.-C. Cheng, A. Bogdanova and A. Bogdanov, *J. Magn. Reson. Imaging*, 1997, **7**, 258–263.
10 F. Cengelli, D. Maysinger, F. Tschudi-Monnet, X. Montet, C. Corot, A. Petri-Fink, H. Hofmann and L. Juillerat-Jeanneret, *J. Pharmacol. Exp. Ther.*, 2006, **318**, 108–116.
11 F. Sonvico, S. p. Mornet, S. b. Vasseur, C. Dubernet, D. Jaillard, J. Degrouard, J. Hoebeke, E. Duguet, P. Colombo and P. Couvreur, *Bioconjugate Chem.*, 2005, **16**, 1181–1188.
12 M. Mahmoudi, A. Simchi, M. Imani and U. O. Halfeli, *J. Phys. Chem. C*, 2009, **113**, 8124–8131.
13 A. Petri-Fink, M. Chastellain, L. Juillerat-Jeanneret, A. Ferrari and H. Hofmann, *Biomaterials*, 2005, **26**, 2685–2694.
14 A. K. Gupta and S. Wells, *IEEE Trans. NanoBiosci.*, 2004, **3**, 66.
15 J. Li, R. Yuan and Y. Chai, *Microchim. Acta*, 2011, **173**, 369–374.
16 J. Wang, Z. Zhu, A. Munir and H. S. Zhou, *Talanta*, 2011, **84**, 783–788.
17 H. Li, Q. Wei, J. He, T. Li, Y. Zhao, Y. Cai, B. Du, Z. Qian and M. Yang, *Biosens. Bioelectron.*, 2011, **26**, 3590–3595.
18 I. M. Hsing, Y. Xu and W. Zhao, *Electroanalysis*, 2007, **19**, 755–768.
19 G. Zhao, J. J. Feng, Q. L. Zhang, S. P. Li and H. Y. Chen, *Chem. Mater.*, 2005, **17**, 3154–3159.
20 H.-H. Yang, S.-Q. Zhang, X.-L. Chen, Z.-X. Zhuang, J.-G. Xu and X.-R. Wang, *Anal. Chem.*, 2004, **76**, 1316–1321.
21 K. Souza, J. Ardisson and E. Sousa, *J. Mater. Sci.: Mater. Med.*, 2009, **20**, 507–512.
22 T. Sen, A. Sebastianelli and I. J. Bruce, *J. Am. Chem. Soc.*, 2006, **128**, 7130–7131.
23 W. Xian-Wen, Z. Guo-Xing, X. Chuan-Jun and Y. Yin, *Nanotechnology*, 2006, **17**, 4307.
24 I. Zhitomirsky, *J. Mater. Sci.*, 2006, **41**, 8186–8195.
25 L. Besra and M. Liu, *Prog. Mater. Sci.*, 2007, **52**, 1–61.
26 Y. S. Kang, S. Risbud, J. F. Rabolt and P. Stroeve, *Chem. Mater.*, 1996, **8**, 2209–2211.
27 T. J. Daou, G. Pourroy, S. Begin-Colin, J. M. Greneche, C. Ulhaq-Bouillet, P. Legare, P. Bernhardt, C. Leuvrey and G. Rogez, *Chem. Mater.*, 2006, **18**, 4399–4404.
28 Y. Li, T. Leng, H. Lin, C. Deng, X. Xu, N. Yao, P. Yang and X. Zhang, *J. Proteome Res.*, 2007, **6**, 4498–4510.
29 X. Shouhu, H. Lingyun, J. Wanquan, G. Xinglong, H. Yuan and C. Zuyao, *Nanotechnology*, 2007, **18**, 035602.
30 J. Li and C.-Y. Liu, *New J. Chem.*, 2009, **33**, 1474–1477.
31 Y. Lu, Y. Yin, B. T. Mayers and Y. Xia, *Nano Lett.*, 2002, **2**, 183–186.

32 Z. X. Sun, F. W. Su, W. Forsling and P. O. Samskog, *J. Colloid Interface Sci.*, 1998, **197**, 151–159.
33 M. Jarlbring, L. Gunneriusson, B. Hussmann and W. Forsling, *J. Colloid Interface Sci.*, 2005, **285**, 212–217.
34 T. J. Daou, G. Pourroy, J. M. Greneche, A. Bertin, D. Felder-Flesch and S. Begin-Colin, *Dalton Trans.*, 2009, 4442–4449.
35 M. L. Fisher, M. Colic, M. P. Rao and F. F. Lange, *J. Am. Ceram. Soc.*, 2001, **84**, 713–718.
36 P. R. Solanki, S. K. Arya, S. P. Singh, M. K. Pandey and B. D. Malhotra, *Sens. Actuators, B*, 2007, **123**, 829–839.
37 Z. Matharu, G. Sumana, S. K. Arya, S. P. Singh, V. Gupta and B. D. Malhotra, *Langmuir*, 2007, **23**, 13188–13192.
38 L. Yonglan, *Mater. Lett.*, 2007, **61**, 1039–1041.
39 L. Huo, W. Li, L. Lu, H. Cui, S. Xi, J. Wang, B. Zhao, Y. Shen and Z. Lu, *Chem. Mater.*, 2000, **12**, 790–794.
40 T. D. Waite and D. M. Sherman, *Am. Mineral.*, 1985, **70**, 1262–1269.
41 T. A. Egerton and I. R. Tooley, *Int. J. Cosmet. Sci.*, 2012, **34**, 117–122.
42 S. L. Westcott, S. J. Oldenburg, T. R. Lee and N. J. Halas, *Langmuir*, 1998, **14**, 5396–5401.
43 Y. Kobayashi, V. Salgueirino-Maceira and L. M. Liz-Marzan, *Chem. Mater.*, 2001, **13**, 1630–1633.
44 K. Tao, H. Dou and K. Sun, *Chem. Mater.*, 2006, **18**, 5273–5278.
45 W. Cai and J. Wan, *J. Colloid Interface Sci.*, 2007, **305**, 366–370.
46 J. Sun, S. Zhou, P. Hou, Y. Yang, J. Weng, X. Li and M. Li, *J. Biomed. Mater. Res., Part A*, 2007, **80**, 333–341.
47 O. N. Shebanova and P. Lazor, *J. Raman Spectrosc.*, 2003, **34**, 845–852.
48 J. Tang, M. Myers, K. A. Bosnick and L. E. Brus, *J. Phys. Chem. B*, 2003, **107**, 7501–7506.
49 W. Feitknecht and K. J. Gallagher, *Nature*, 1970, **228**, 548–549.
50 J. Morales, L. Sanchez, F. Martin, F. Berry and X. L. Ren, *J. Electrochem. Soc.*, 2005, **152**, A1748–A1754.
51 P. Guardia, J. Perez-Juste, A. Labarta, X. Batlle and L. M. Liz-Marzan, *Chem. Commun.*, 2011, **46**, 6108–6110.
52 B. M. Kabyemela, T. Adschiri, R. M. Malaluan and K. Arai, *Ind. Eng. Chem. Res.*, 1999, **38**, 2888–2895.
53 Q. Wang, H. Li, L. Chen and X. Huang, *Carbon*, 2001, **39**, 2211–2214.
54 C. Adina, F. Florinela, T. Abdelmoumen and S. Carmen, *Rom. Biotechnol. Lett.*, 2010, **15**, 5738–5744.
55 A. Azioune, A. Ben Slimane, L. Ait Hamou, A. Pleuvy, M. M. Chehimi, C. Perruchot and S. P. Armes, *Langmuir*, 2004, **20**, 3350–3356.
56 D. Kandpal, S. Kalele and S. Kulkarni, *Pramana*, 2007, **69**, 277–283.
57 P. Pramod, S. T. S. Joseph and K. G. Thomas, *J. Am. Chem. Soc.*, 2007, **129**, 6712–6713.
58 Z. Matharu, P. Pandey, M. K. Pandey, V. Gupta and B. D. Malhotra, *Electroanalysis*, 2009, **21**, 1587–1596.
59 T. Sen, A. Sebastianelli and I. J. Bruce, *J. Am. Chem. Soc.*, 2006, **128**, 7130–7131.
60 J. L. Campbell, J. Arora, S. F. Cowell, A. Garg, P. Eu, S. K. Bhargava and V. Bansal, *PLoS One*, 2011, **6**, e21857.
61 L. L. Vatta, J. Kramer and K. R. Koch, *Sep. Sci. Technol.*, 2007, **42**, 1985–2002.
62 A. A. Ansari, A. Kaushik, P. R. Solanki and B. D. Malhotra, *Electrochem. Commun.*, 2008, **10**, 1246–1249.
63 A. A. Ansari, A. Kaushik, P. R. Solanki and B. D. Malhotra, *Electroanalysis*, 2009, **21**, 965–972.
64 S. P. Singh, S. K. Arya, P. Pandey, B. D. Malhotra, S. Saha, K. Sreenivas and V. Gupta, *Appl. Phys. Lett.*, 2007, **91**, 063901–063903.
65 P. R. Solanki, A. Kaushik, A. A. Ansari and B. D. Malhotra, *Appl. Phys. Lett.*, 2009, **94**, 143901–143903.
66 G. Kouassi, J. Irudayaraj and G. McCarty, *J. Nanobiotechnol.*, 2005, **3**, 1.

 